

Enhanced sensitivity of sub-THz thermomechanical bolometers exploiting vibrational nonlinearity

L. Alborghetti,¹ B. Bertoni,^{1,2} L. Vicarelli,¹ S. Zanotto,² S. Roddaro,^{1,2} A. Tredicucci,^{1,2} M. Cautero,³ L. Gregorat,⁴ G. Cautero,⁵ M. Cojocari,⁶ G. Fedorov,⁶ P. Kuzhir,⁶ and A. Pitanti^{1,2}

¹*Department of Physics, University of Pisa, Largo B. Pontecorvo 3, 56127 Pisa - Italy*

²*NEST, CNR Istituto Nanoscienze, piazza San Silvestro 12, 56127 Pisa - Italy**

³*Department of Physics, Università degli Studi di Trieste, Via Alfonso Valerio 2, 34127 Trieste, Italy*

⁴*Department of Engineering and Architecture, Università degli Studi di Trieste, Via Alfonso Valerio 6/1, 34127 Trieste, Italy*

⁵*Elettra - Sincrotrone Trieste S.C.p.A., Strada Statale 14, km 163.5, 34149 Trieste, Italy*

⁶*Department of Physics and Mathematics, Center of Photonics Research, University of Eastern Finland, Yliopistokatu 7, FI-80101 Joensuu, Finland*

A common approach to detecting weak signals or minute quantities involves leveraging on the localized spectral features of resonant modes, where sharper lines (i.e. high Q-factors) enhance transduction sensitivity. However, maximizing the Q-factor often introduced technical challenges in fabrication and design. In this work, we propose an alternative strategy to achieve sharper spectral features by using interference and nonlinearity, all while maintaining a constant dissipation rate. Using far-infrared thermomechanical detectors as a test case, we demonstrate that signal transduction along an engineered response curve slope effectively reduces the detector’s noise equivalent power (NEP). This method, combined with an optimized absorbing layer, achieves sub-pW NEP for electrical read-out detectors operating in the sub-THz range.

I. INTRODUCTION

Transducer-based sensing – relying on the conversion of energy from one form (the measured quantity) to another (read-out signal) – strongly benefits from spectrally sharp transfer functions, as large derivatives translates into large responsivities. The usual route for optimizing the transfer functions relies on devising resonant elements with low energy loss rates; this manifests into narrow linewidths (large Q-factors) and leads to large sensitivities, which have been widely and successfully employed among the others in mass [1], aerostatic pressure [2], gas [3], temperature [4], polarization state [5] and refractive index [6] sensing. Increasing the Q-factors of nano- and micro-metric sized detectors, whose footprint is suitable for integration in electronic systems, represents a significant technological challenge, both in terms of design and fabrication. Noteworthy, an intense research has recently led to ultra-high Q-factors (exceeding one billion) in micromechanical resonators oscillating at frequencies from hundreds of kHz to MHz, obtained through soft clamping and dissipation dilution design as well as careful fabrication [7–10]. Although impressive, reaching consistently these values in commercially compatible processes remains a significant challenge: device imperfections or intrinsic physical effects often create bottlenecks, ultimately limiting the maximum sensitivity of commercial devices, which routinely have Q-factor ranging around 10^4 - 10^5 . A different, interesting route to obtain sharp features in the transfer functions relies on manipulating the resonant lineshape, creating steeper edges while maintaining

the same energy loss rate. To this end, Fano-induced asymmetry has been used for sensing enhancement, showing promising results for gas [11–13], refractive index [14, 15] and temperature [16] sensing.

Improvements based on exploiting Fano lineshapes are still restricted by the limited manipulation of the Fano factor, which usually depends on the coupling between a broad and a narrow linewidth cavity system [17]. Moreover, the maximum slope of a Fano response function is still connected to the resonator’s Q-factor. This further limit can be surpassed by taking advantage of the intrinsic device nonlinearities, which can produce massive linewidth deformations (foldover effect [18]) or lead to multistability [19], with internal transitions between stable solutions leading to, in principle, “infinitely sharp” spectral features.

These concepts have been successfully implemented in several systems including superconductor [20] and semiconductor [21, 22] based single photon detectors. They also have focused applications in micromechanical systems, including mass sensors monitoring the shift of nonlinear resonant frequencies [23, 24], “threshold-based” sensors exploiting bifurcation phenomena for mass [25, 26] and gas [27, 28] limit detection, as well as more structured platforms exploiting exceptional points [29].

In this paper, we show how nonlinear transduction sensing can be employed to enhance the characteristics of far-infrared light detectors based on thermo-mechanical bolometers (TMBs). TMBs have recently emerged as a powerful technology which offers broadband detection at room-temperature, with single-pixel operation at video-rate and faster [30–34] and the possibility of scaling up the system to focal plane arrays for multiplexed imaging applications [35, 36]. The best TMB devices

* benedetta.bertoni@phd.unipi.it

have a noise-equivalent power (NEP) in a range from a few $\text{pW}/\sqrt{\text{Hz}}$ level, to less than $100 \text{ pW}/\sqrt{\text{Hz}}$, already outperforming some of the commercially available technologies [37].

Our approach to TMBs makes use of silicon nitride (Si_3N_4) trampoline resonators, which have previously shown a NEP of about $100 \text{ pW}/\sqrt{\text{Hz}}$ at 20 Hz operating speed in a $1 \times 1 \text{ mm}$ sided membrane, illuminated with a 140 GHz source and optically read out via self-mixing interferometry [32].

Compared to our previous results, the devices here investigated have a reduced pixel size and employ specific layers for improved absorptance. In addition, addressing the TMB with metallic wires in a magnetic field, we switched to all-electrical probing via inductive read-out [38], which, respect to the cumbersome optical readout, is better suited for integration and parallelization in large-scale arrays.

Finally, we exploited the material Duffing nonlinearity [39], an effect arising when the restoring force no longer follows Hooke’s law at high levels of strain, leading to an anharmonic response. By applying nonlinear transduction schemes, we achieve an ultrasmall NEP of about $0.1 \text{ pW}/\sqrt{\text{Hz}}$ in a narrow bandwidth, evaluated under an illuminating 140 GHz source and at room temperature. Combined with an operating speed of 40 Hz, our device characteristics and measurement technique challenge the state of the art for room-temperature bolometric detectors in the sub-THz range.

II. METHODS

A. Device details

The devices were based on Si_3N_4 trampoline membrane resonators, which in the last decade have been successfully employed for classical sensing [40] and quantum applications [41, 42]. The basic device geometry consisted of single membranes made of a 300 nm thick stoichiometric silicon nitride, with a $100 \times 100 \mu\text{m}$ central plate hanging on a $300 \times 300 \mu\text{m}$ frame through four 12 μm wide tethers. All membranes had Cr/Au metallic contacts running through the tethers. These granted for a practical all-electrical read-out and actuation [38, 43, 44] employing inductive reading or Lorentz force, respectively, enabled by a 250 mT magnetic field induced by static Nd magnets. A scanning electron micrograph of a typical device is reported in **Figure 1** (a) along with a sketch outlining the read-out circuit. In order to enhance the device absorbance without degrading its mechanical properties, we introduced “ultra-light” bidimensional layers in the center of the membrane. We have explored the implementation of both metallic and carbon-based absorbers [45]. The choice for the metal was a Cr/Au bilayer with an overall thickness of about 8 nanometers. At such a small thickness scale the metal layer will be a non-uniform

film composed by adjacent grains, increasing its sheet resistance compared to its bulk metal value and favouring the approach to the limit value of 188Ω which would nominally give perfect impedance matching and the theoretical 50% absorption limit for an isolated layer [46]. Another interesting avenue made use of amorphous carbon materials which can be directly grown on silicon nitride via chemical vapour deposition [47, 48], allowing fine adjustments of the layer conductivity through the precise control of the film thickness. The material of our choice, pyrolytic carbon (PyC), has shown an impressive absorption of $\sim 43\%$ in the sub-THz range [49]. Therefore, we realized and investigated two different device implementations, with the same nominal geometrical parameters for the trampoline resonator and different absorbing layers, namely a 2/6 nm Cr/Au thick layer (**Au device**) and a 18 nm pyrolytic carbon thick layer (**PyC device**), respectively.

B. Detector read-out

The devices were mounted on a ceramic piezoelectric stack actuator (PZT) layer which was used to coherently excite the membrane motion (see **Figure 1** (a)). The AC drive voltage applied on the actuator was generated by the reference channel of a lock-in amplifier (LIA), whose input channel was connected to the TMB contact to sense the magnetomotive voltage ΔV , induced by the modulation of the concatenated magnetic flux due to the vibrational displacement. TMB, actuator and static magnets were placed on a custom-made printed circuit board; this was inserted in a vacuum chamber to reduce atmospheric viscous damping. Optical access was enabled through a cyclic olefin copolymer (COC) window. The vacuum chamber was additionally mounted on a planar moving stage (xy plane), used to scan the TMB position for extended imaging. The illumination was done via a continuous wave, 30 mW, 140 GHz source focused on the device with two parabolic mirrors (not shown in the sketch of **Figure 1** (a)).

The concept behind the detection mechanism lies in the shift of the resonant frequency of specific mechanical modes due to thermally induced device deformations, namely thermal expansion and tensile stress reduction. The temperature change is conversely caused by the absorption of the electromagnetic radiation which one wants to detect. Sweeping the driving frequency, it is possible to directly acquire the whole mechanical spectrum and evaluate the frequency shift Δf of specific features of the “bright” spectrum (A_b) from the “dark” (A_d) one (Spectral Scan, see **Figure 1** (c)). In our operating conditions the frequency shift scales linearly with the illuminating intensity, granting the use of this operating mode with signals with large dynamic ranges and enabling its use for the direct acquisition

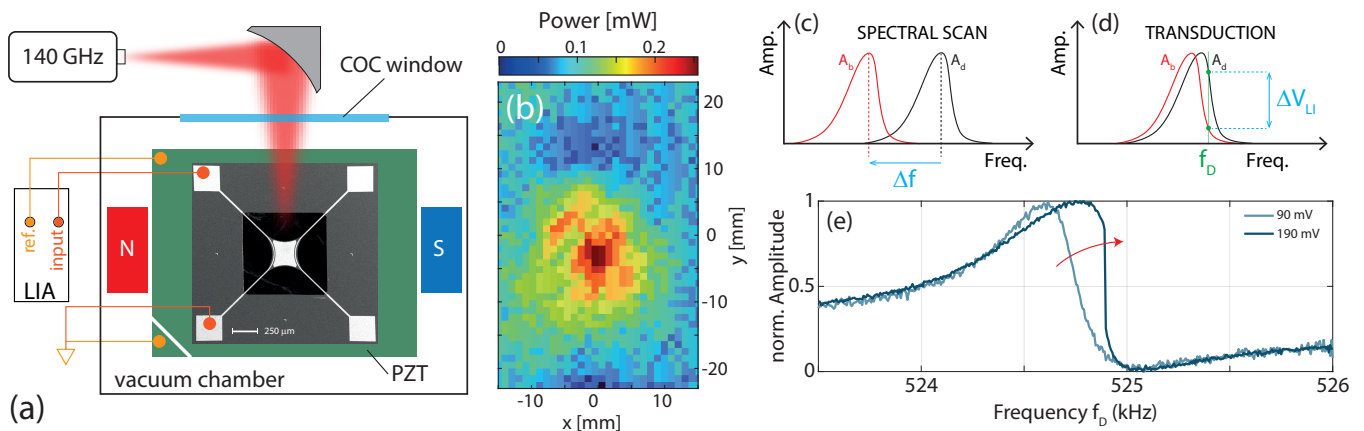


FIG. 1. (a): Sketch of the experimental setup along with a SEM micrograph of one typical TMB. The device sits on a piezoelectric actuator stack (PZT) in a vacuum chamber with optical access via a cyclic olefin copolymer (COC) window. Static magnets generate a planar magnetic field which is used for the coherent magneto-motive read-out demodulated by a lock-in amplifier (LIA) at the forcing mechanical drive. (b): Beam profiling of the 140 GHz source. Comparison of the Spectral Scan (c) and Transduction (d) operating modes. (e): Distortion of the resonance lineshape of the trampoline resonator by increasing the driving amplitude and entering strong nonlinear motional regimes.

of images, as reported, for example, in **Figure 1** (b), where the source focused beam profile has been imaged via spatial scan. The linear response allows a direct conversion of the image from frequency shift to impinging power; here this was done by imposing the proper beam normalization to its total power, which has been independently measured through a calibrated Goly cell detector. Note that the spectral scan is a generally slow detection method, often limited by the slow acquisition time with lock-in amplifier due to the long frequency sweeps, especially when multiple devices are simultaneously investigated.

Faster detection protocols with a reduced dynamic range rely instead on operating with a single frequency demodulating tone f_D and exploiting the transduction effect in an open-loop configuration, as illustrated in the transduction scheme of **Figure 1** (d). In our device, the transduction detection speed can reach video-rate [32], limited by the thermal relaxation through the tethers. This process, with Q-factors for our devices ranging between 10^3 and 10^5 , fully dominates the dynamics of the entire TMB upon illumination. In the transduction scheme, the frequency shift is directly converted in a read-out voltage ΔV_{LI} which depends on the difference between dark and bright spectrum amplitudes at f_D , $A_d(f_D)$ and $A_b(f_D)$, respectively. For the detection of weak signals, the bright spectrum can be recast as a frequency shift of the dark spectrum by a vanishing δf , obtaining:

$$\Delta V_{LI} \sim A_d(f_D) - A_d(f_D + \delta f) \sim \left. \frac{dA_d}{df} \right|_{f=f_D} \delta f \quad (1)$$

and giving a read-out voltage directly proportional to the first derivative of the spectral amplitude at f_D . Changing f_D allows one to explore different regions of the signal

derivative, which can be very large in asymmetric and nonlinear resonances. In particular, our resonance shows both Fano interference and nonlinear hardening due to the Duffing effect, which is known to produce an increase in the steepness of the spectral features. This is shown in **Figure 1** (e), which displays typical resonance lineshapes of a **PyC** device at different driving strengths: one can see that the asymmetric Fano resonance becomes steeper around 525 kHz due to the Duffing effect at an increased driving voltage amplitude.

III. SPECTRAL TRANSDUCTION

We evaluated the effect of asymmetric lineshapes on the figure of merit of transduction experiments with our TMB devices. Typical amplitude spectra of the **PyC** device, demodulated with a sweeping mechanical driving voltage of 190 mV and with on/off source respectively are shown in **Figure 2**.

Leveraging on the intensity map of **Figure 1** (b), we estimated the radiation power illuminating the detector. Considering the small size of our “pixel” compared to the diffraction limited area at this wavelength, i.e. $\lambda^2/4 \approx 1.15 \text{ mm}^2$, we considered the latter as the effective detection area [32], obtaining an effective illuminating power of $P_i \sim 0.1 \text{ mW}$.

Operating the device in transduction mode and considering a weak signal approximation, a static responsivity can be defined for each driving frequency f_D as:

$$R_s(f_D) \sim \left. \frac{dV_{LI}}{df} \right|_{f=f_D} \left(\frac{\Delta f}{P_i} \right) \quad (2)$$

where the static spectral shift per unit power $\Delta f/P_i$ can be estimated from the results of **Fig 2** (a). The dy-

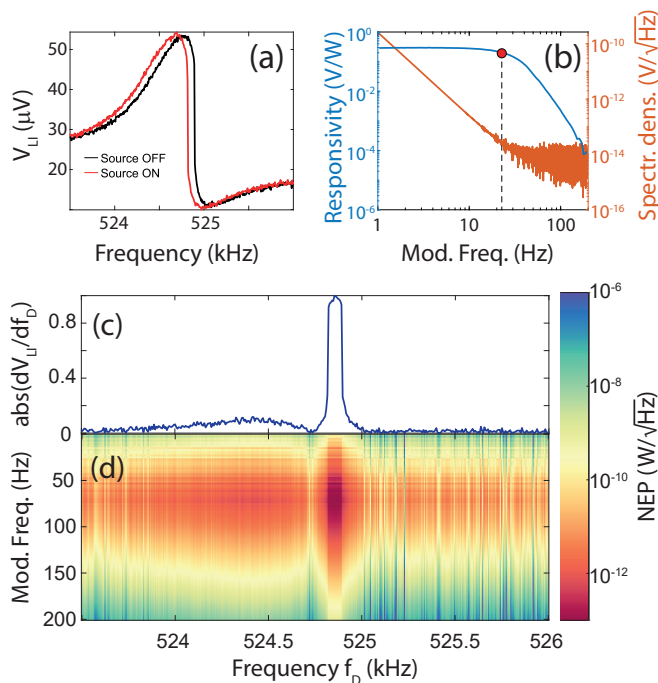


FIG. 2. (a): typical ON/OFF spectra for the **PyC device** with a 190 mV piezo driving voltage. (b): device responsivity and noise spectral density in the dark condition. (c): normalized derivative of the modulus of the OFF spectrum reported in (a). (d): spectrogram of PyC device NEP. The minimum NEP can be found around 524.8 kHz for a modulation frequency of 40 Hz.

dynamic responsivity R was then evaluated by combining the previous results with the Bode frequency response, obtained using square wave modulation of the source in a frequency range f_M from 1 to 120 Hz, with an external electrical signal provided by the LIA. A typical dynamic responsivity measured at a driving frequency of 524.8 kHz is reported in the left axis of **Figure 2** (b). From the Bode plot we can extract a cut-off frequency of about 20 Hz, defined as the -3 dB drop of the signal amplitude, indicated by a red dot in **Figure 2** (b).

Next, the device noise spectral density was measured in dark conditions, in the same range of the Bode plot, using the spectral analyzer tool within the lock-in amplifier (UHF 600 MHz Zurich Instruments). A typical measurement is reported on the right axis of **Figure 2** (b). The need to operate around the mechanical frequency imposes the injection of a frequency tone to the oscillator; its phase noise leakage represents the main component of the noise spectral density. Its slope of $\propto f^{-3}$ confirms the dominant flicker noise component, as expected from the Leeson's equation [50]. Other noise contributions can likely originate from the crosstalk in the device electrical connections. Finally, the ratio of noise spectral density to the dynamic responsivity gives an estimate of the Noise-Equivalent power, which in our case is a spectral function of both the modulating frequency f_M and

driving frequency f_D , which selects the resonance spectral feature used for transduction.

The full NEP spectrogram for the **PyC device** excited with a 190 mV driving tone has been reported in **Figure 2** (d). It is significant to observe that, at each driving frequency f_D , the NEP has a minimum around 40 Hz, giving a good operational speed of our device, when compared with a previous report where slightly larger detectors were considered [32]. Additionally, we notice a drastic reduction of the NEP at a driving frequency of $f_D=524.8$ kHz, reaching a value below $1 \text{ pW}/\sqrt{\text{Hz}}$, significantly reduced with respect to the rest of the spectrum. Unsurprisingly, this f_D corresponds to the spectral region with the highest slope, as can be seen from **Figure 2** (c), where we reported the normalized modulus of the derivative calculated from the result of **Figure 2** (a). Qualitatively similar effects are present at different driving voltages: higher drives lead to even sharper line-shapes, with a corresponding decrease in the NEP in very narrow spectral regions. Conversely, lower drives produce an increase in the NEP, although with a consistently low value found in a broader spectral range. The latter is linked to the device dynamic range of operation: large spectral regions with significant slopes are most beneficial for using the detector for imaging or as a power meter; at the other limit, with a point-like extremely large slope, we expect the device to operate as a threshold-switching detector, better suited for the recognition of single events (i.e. laser pulses), as will be discussed later.

In our operating scheme, the device characteristics can be indeed estimated by directly looking at the derivative of the resonance. **Figure 3** (a) shows the normalized mechanical spectrum of the **PyC device** under a driving voltage of 90 mV; although less pronounced with respect to the data of **Figure 2**, this excitation configuration still gives a strong asymmetry, spanning from a combination of interference and material nonlinearities. The asymmetry can be made even more manifest by looking at the derivative: the largest negative slope is about 5 times the largest positive one, see the green dots and lines in **Figure 3** (b). The **Au device** shows a qualitatively similar asymmetry, as shown in **Figure 3** (c-d), with some differences given by the different experimental assembly resulting in a different Fano factor and a different resonating frequency. For a fair comparison between the devices, we considered the driving strength leading to the bifurcation point (discussed in more detail later) which, for device made of similar material and resonating at a similar complex frequency, translates into having the same vibrational amplitude. From this normalization we rescaled the driving voltage of the **Au device** to 40 mV (**Figure 3** (c-d)), so that it can be compared to the 90 mV drive of the PyC one (**Figure 3** (a-b)). The **Au device** also exhibits a strong asymmetry (roughly a 1.6 times increase of the negative to the positive slope) and generally larger derivative with respect to the PyC device.

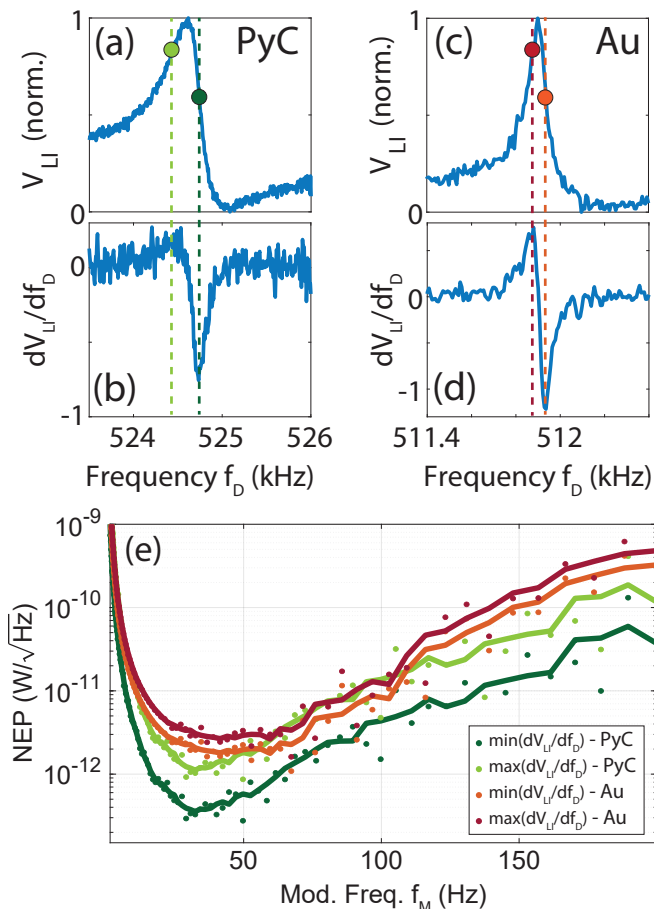


FIG. 3. Normalized vibrational spectrum (a) and its first derivative (b) of the PyC device. Normalized vibrational spectrum (c) and its first derivative (d) of the Au device. The dashed lines indicate in both cases the position of the maximum and minimum derivative, respectively. (e): experimental data points along with interpolated lines illustrating the NEP estimated at the maximum and minimum of the derivative for both devices.

The NEP evaluated by setting f_D at the maximum and minimum slopes of both devices is reported in **Figure 3** (e) as a function of the modulation frequency of the 140 GHz source. All the NEP curves have a minimum around 40 - 50 Hz, consistent with the results of **Figure 2** (d), and show an overall good value which strongly depends of the chosen transducing frequency. In fact, for both devices, the NEP linearly scales with the derivative, as expected from **Eq. (2)**, resulting in a net enhancements of about a factor of 4 and 1.5, respectively, in good agreement with what expected from the derivatives. Note that the enhancements are within the same mechanical spectrum, obtained just by changing f_D .

Moreover, the **PyC device** shows about an order of magnitude improvement with respect to the **Au device**. This originates from the different absorbance of the two materials at 140 GHz; interestingly, comparing the best NEP values in the two devices, opportunely rescaled

to account for the different slopes, gives an absorption-induced enhancement of ~ 3.74 , in good agreement with the scaling of the static responsivities estimated as $R_s^{PyC} \sim 1042$ kHz/W and $R_s^{Au} \sim 278$ kHz/W, giving $R_s^{PyC}/R_s^{Au} = 3.75$. From this observation, we can estimate the absorbance of the metallic layer, starting from an experimentally measured PyC film absorbance of 40% in the far-infrared range [49]. The obtained Cr/Au absorbance of $\sim 10\%$ is compatible with a simple multilayer simulation using experimentally estimated refractive indices [51], which returns a numerical value of $4 \pm 0.5\%$ for a continuous film, whereas we expect a further enhancement due to the layer inhomogeneity. The best NEP we obtained reaches 0.2 pW/ $\sqrt{\text{Hz}}$, entering the range of state-of-the-art diode [52, 53] and transistor [54–56] detectors, at the expense of a slower operating speed and reduced dynamic range. As a more quantitative example, with the driving condition of **Figure 3**, the **PyC device** negative derivative peak has a linewidth of about 150 Hz, limiting its use to weak signals with power less than roughly 140 nW, as estimated by considering the spectral static device responsivity.

A further increase of the driving voltage leads the system to highly nonlinear regimes which, in the case of Duffing nonlinearities, can eventually reach multistable or chaotic motion [39]. As an example, **Figure 4** (a-b) reports the comparison of an asymmetric, single-solution resonance (red curve) and a regime past the bifurcation point (blue curve) for both devices under investigation. The multistable regime can be characterized by abrupt jumps resulting from the switching between two dynamical solutions, which can be clearly identified in both the **PyC device** and **Au device**. The onset of multistability essentially depends on the vibrational amplitude, since the Duffing nonlinearity enters the equation of motion with a cubic displacement term [36]. The bifurcation point from a single to multiple dynamical solution has been taken as a common reference to compare both devices.

One can think of the switching as a “line with infinite slope”, which looks appealing for transduction detection. Unfortunately, in this case the derivative tends to a δ -function, as can be seen from the ones reported in **Figure 4** (c-d), respectively. Evaluating the figures (and the insets for the full range of the y axis), one can expect an extreme enhancement of device performance in terms of responsivity, which comes along with a vanishing dynamic range.

Since it operates at a single frequency point, this particular regime of operation does not grant a use for the device as an imaging or power meter detector; conversely it looks promising for a threshold-based detector, where the discontinuity in the read-out can be triggered by specific events over a certain limit (i.e. single photons, light pulse detection, temperature change, mass loading). In a scheme similar to the superconducting optical

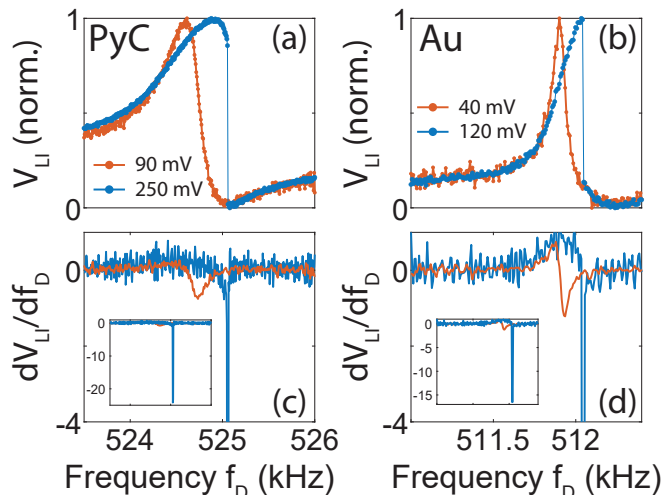


FIG. 4. Normalized vibrational spectrum (a) of the PyC device under a weak (90 mV) and a strong (250 mV) driving voltage amplitude, respectively. The large drive amplitude leads to a multistable regime where the oscillator jumps from one stable solution to the other. The multistability leads to delta-like responsivity, as seen in the zoomed-in calculated first derivative of (c) (inset: full scale derivative comparison). (b,d): Similar measurements for the Au device.

detectors [20] or bifurcation-based sensors [25–29] in other nonlinear systems, this operating regime adds to the potential and possibilities lying in thermomechanical bolometer devices.

IV. CONCLUSION

While increasing the quality factor in resonant detectors generally enhances device performance, consistently achieving high values can be challenging, especially in the context of mass production for real-world applications. In this work, we presented an alternative approach to locally achieve high responsivity and low NEP in transduction detection experiments by exploiting device nonlinearities.

Through careful characterization of thermomechanical bolometers, we demonstrated that the device NEP under 140 GHz illumination is strongly dependent on the driving strength and transduction frequencies. In the optimal operating range, we achieved a sub-pW/ $\sqrt{\text{Hz}}$ NEP for a TMB employing pyrolytic carbon as an absorbing layer, which exhibited an impressive 40% absorbance in just an 18 nm thick layer [49].

This carbon-based material also offers additional advantages: not only it is chemically inert, but its thickness and thus its AC conductivity and absorption capability can be conveniently controlled by tuning the synthesis conditions [57].

With a 40 Hz operating speed, our device offers a powerful tool for power detection of low-intensity signals.

Given that the increase of the trampoline temperature exposed to electromagnetic radiation is based on broad band absorption in a thin conductive layer (PyC or Au) we expect our approach to provide as good performance for detection of radiation up to 10 THz.

Additionally, by further increasing the driving strength and entering a highly nonlinear regime, we propose leveraging the same platform for threshold signal detection. In this regime, the system can transition between stable solutions in response to external perturbations of sufficient magnitude, similar to superconducting or bifurcation-based detectors, opening up further possibilities for our technology.

Acknowledgements

The authors gratefully acknowledge funding from ATTRACT, a European Union’s Horizon 2020 research and innovation project under grant agreement No. 101004462 (H-cube project), from European Union - Next Generation EU under the Italian National Recovery and Resilience Plan (NRRP), Mission 4, Component 2, Investment 1.3, CUP D43C22003080001, partnership on “Telecommunications of the Future” (PE00000001 - program “RESTART”) and from MUR through the project PRIN 2022 TRUST. This work is supported by the Academy of Finland via Flagship Programme Photonics Research and Innovation (PREIN), decision 320166, Horizon 2020 RISE CHARTIST project 101007896, Horizon 2020 RISE TERASSE project 823878.

-
- [1] T. Ikehara, J. Lu, M. Kommo, R. Maeda, and T. Mihara. A high quality-factor silicon cantilever for a low detection-limit resonant mass sensor operated in air. *J. Micromech. Microeng.*, 17(12):2491, November 2007.
- [2] Yong Yang, Sunny Saurabh, Jonathan M Ward, and Sile Nic Chormaic. High-q, ultrathin-walled microbubble resonator for aerostatic pressure sensing. *Optics express*, 24(1):294–299, 2016.
- [3] Tao Chen, Zhanghua Han, Jianjun Liu, and Zhi Hong. Terahertz gas sensing based on a simple one-dimensional photonic crystal cavity with high-quality factors. *Appl.*

- Opt.*, *AO*, 53(16):3454–3458, June 2014.
- [4] Jesús Sánchez-Pastor, Petr Kaděra, Masoud Sakaki, Rolf Jakoby, Jaroslav Lacik, Niels Benson, and Alejandro Jiménez-Sáez. A wireless w-band 3d-printed temperature sensor based on a three-dimensional photonic crystal operating beyond 1000° c. *Communications Engineering*, 3(1):137, 2024.
- [5] Simone Zanotto, Alessandro Tredicucci, Daniel Navarro-Urrios, Marco Cecchini, Giorgio Biasiol, Davide Mencarelli, Luca Pierantoni, and Alessandro Pitanti. Optomechanics of chiral dielectric metasurfaces. *Advanced Opti-*

- cal Materials*, 8(4):1901507, 2020.
- [6] Daquan Yang, Huiping Tian, and Yuefeng Ji. High-Q and high-sensitivity width-modulated photonic crystal single nanobeam air-mode cavity for refractive index sensing. *Appl. Opt., AO*, 54(1):1–5, January 2015.
 - [7] Dennis Høj, Fengwen Wang, Wenjun Gao, Ulrich Busk Hoff, Ole Sigmund, and Ulrik Lund Andersen. Ultra-coherent nanomechanical resonators based on inverse design. *Nature communications*, 12(1):5766, 2021.
 - [8] Yeghishe Tsaturyan, Andreas Barg, Eugene S Polzik, and Albert Schliesser. Ultracoherent nanomechanical resonators via soft clamping and dissipation dilution. *Nature nanotechnology*, 12(8):776–783, 2017.
 - [9] Nils Johan Engelsen, Alberto Beccari, and Tobias Jan Kippenberg. Ultrahigh-quality-factor micro-and nanomechanical resonators using dissipation dilution. *Nature Nanotechnology*, pages 1–13, 2024.
 - [10] Andrea Cupertino, Dongil Shin, Leo Guo, Peter G Steeneken, Miguel A Bessa, and Richard A Norte. Centimeter-scale nanomechanical resonators with low dissipation. *Nature Communications*, 15(1):4255, 2024.
 - [11] Shrouk E. Zaki and Mohamed A. Basyooni. Ultra-sensitive gas sensor based fano resonance modes in periodic and fibonacci quasi-periodic Pt/PtS₂ structures. *Sci Rep*, 12(1):9759, June 2022.
 - [12] Sherif M. Sherif and Mohamed A. Swillam. Silicon-based mid infrared on-chip gas sensor using Fano resonance of coupled plasmonic microcavities. *Sci Rep*, 13(1):12311, July 2023.
 - [13] Shrouk E. Zaki, Ahmed Mehaney, Hekmat M. Hassanein, and Arafa H. Aly. Fano resonance based defect 1D phononic crystal for highly sensitive gas sensing applications. *Sci Rep*, 10(1):17979, October 2020.
 - [14] Jun Zhu and Changsong Wu. Optical refractive index sensor with Fano resonance based on original MIM waveguide structure. *Results in Physics*, 21:103858, February 2021.
 - [15] Yue Tang, Zhidong Zhang, Ruibing Wang, Zhenyin Hai, Chenyang Xue, Wendong Zhang, and Shubin Yan. Refractive index sensor based on fano resonances in metal-insulator-metal waveguides coupled with resonators. *Sensors*, 17(4):784, 2017.
 - [16] Yan Kong, Qi Wei, Cheng Liu, and Shouyu Wang. Nanoscale temperature sensor based on Fano resonance in metal-insulator-metal waveguide. *Optics Communications*, 384:85–88, February 2017.
 - [17] Mikhail F Limonov, Mikhail V Rybin, Alexander N Poddubny, and Yuri S Kivshar. Fano resonances in photonics. *Nature photonics*, 11(9):543–554, 2017.
 - [18] Jianhua Yang, S Rajasekar, and Miguel AF Sanjuán. Vibrational resonance: A review. *Physics Reports*, 1067:1–62, 2024.
 - [19] Viet-Thanh Pham, Sundarapandian Vaidyanathan, and Tomasz Kapitaniak. Complexity, dynamics, control, and applications of nonlinear systems with multistability. *Complexity*, 2020, 2020.
 - [20] Iman Esmaeil Zadeh, J Chang, Johannes WN Los, Samuel Gyger, Ali W Elshaari, Stephan Steinhauer, Sander N Dorenbos, and Val Zwiller. Superconducting nanowire single-photon detectors: A perspective on evolution, state-of-the-art, future developments, and applications. *Applied Physics Letters*, 118(19), 2021.
 - [21] Andreas Pfenning, Sebastian Krüger, Fauzia Jabeen, Lukas Worschech, Fabian Hartmann, and Sven Höfling. Single-photon counting with semiconductor resonant tunneling devices. *Nanomaterials*, 12(14):2358, 2022.
 - [22] JC Blakesley, P See, AJ Shields, BE Kardynał, P Atkinson, I Farrer, and DA Ritchie. Efficient single photon detection by quantum dot resonant tunneling diodes. *Physical review letters*, 94(6):067401, 2005.
 - [23] Mai Duc Dai, Kilho Eom, and Chang-Wan Kim. Nanomechanical mass detection using nonlinear oscillations. *Applied Physics Letters*, 95(20):203104, November 2009.
 - [24] Mai Duc Dai, Chang-Wan Kim, and Kilho Eom. Nonlinear vibration behavior of graphene resonators and their applications in sensitive mass detection. *Nanoscale research letters*, 7:1–10, 2012.
 - [25] Vijay Kumar, Yushi Yang, J William Boley, George T-C Chiu, and Jeffrey F Rhoads. Modeling, analysis, and experimental validation of a bifurcation-based microsensor. *Journal of microelectromechanical systems*, 21(3):549–558, 2012.
 - [26] Mert Yuksel, Ezgi Orhan, Cenk Yanik, Atakan B Ari, Alper Demir, and M Selim Hanay. Nonlinear nanomechanical mass spectrometry at the single-nanoparticle level. *Nano letters*, 19(6):3583–3589, 2019.
 - [27] M. S. Al-Ghamdi, M. E. Khater, K. M. E. Stewart, A. Alneamy, E. M. Abdel-Rahman, and A. Penlidis. Dynamic bifurcation MEMS gas sensors. *J. Micromech. Microeng.*, 29(1):015005, November 2018.
 - [28] Yasser S Shama, Sasan Rahmanian, Hamza Mouharar, Rana Abdelrahman, Alaaeldin Elhady, and Eihab M Abdel-Rahman. Unraveling the nature of sensing in electrostatic mems gas sensors. *Microsystems & Nanoengineering*, 10(1):56, 2024.
 - [29] Man-Na Zhang, Lei Dong, Li-Feng Wang, and Qing-An Huang. Exceptional points enhance sensing in silicon micromechanical resonators. *Microsystems & Nanoengineering*, 10(1):12, 2024.
 - [30] Andrew Blaikie, David Miller, and Benjamín J Alemán. A fast and sensitive room-temperature graphene nanomechanical bolometer. *Nature communications*, 10(1):4726, 2019.
 - [31] Y. Zhang, S. Hosono, N. Nagai, and K. Song S.-H., Hirakawa. Fast and sensitive bolometric terahertz detection at room temperature through thermomechanical transduction. *J. Appl. Phys.*, 125:151602, 2019.
 - [32] Leonardo Vicarelli, Alessandro Tredicucci, and Alessandro Pitanti. Micromechanical Bolometers for Subterahertz Detection at Room Temperature. *ACS Photonics*, 9(2):360–367, February 2022.
 - [33] Markus Piller, Johannes Hiesberger, Elisabeth Wistrela, Paolo Martini, Niklas Luhmann, and Silvan Schmid. Thermal ir detection with nanoelectromechanical silicon nitride trampoline resonators. *IEEE Sensors Journal*, 23(2):1066–1071, 2022.
 - [34] Chang Zhang, Eeswar K Yalavarthi, Mathieu Giroux, Wei Cui, Michel Stephan, Ali Maleki, Arnaud Weck, Jean-Michel Ménard, and Raphael St-Gelais. High detectivity terahertz radiation sensing using frequency-noise-optimized nanomechanical resonators. *arXiv preprint arXiv:2401.16503*, 2024.
 - [35] Laurent Duraffourg, Ludovic Laurent, Jean-Sébastien Moullet, Julien Arcamone, and Jean-Jacques Yon. Array of resonant electromechanical nanosystems: A technological breakthrough for uncooled infrared imaging. *Micro-machines*, 9(8):401, 2018.

- [36] L. Gregorat, M. Cautero, L. Vicarelli, D. Giuressi, A. Bagolini, A. Tredicucci, G. Cautero, and A. Pitanti. Highly dispersive multiplexed micromechanical device array for spatially resolved sensing and actuation. *Microsyst. Nanoeng.*, 2024.
- [37] Chao Li, Ya Zhang, and Kazuhiko Hirakawa. Terahertz Detectors Using Microelectromechanical System Resonators. *Sensors*, 23(13):5938, January 2023.
- [38] Silvan Schmid, Luis Guillermo Villanueva, and Michael Lee Roukes. *Fundamentals of nanomechanical resonators*, volume 49. Springer, 2016.
- [39] Heinz Georg Schuster. *Reviews of nonlinear dynamics and complexity*. Wiley Online Library, 2008.
- [40] Kostas Kanellopoulos, Friedrich Ladinig, Stefan Emminger, Paolo Martini, Robert G West, and Silvan Schmid. Comparative analysis of nanomechanical resonators: Sensitivity, response time, and practical considerations in photothermal sensing. *arXiv preprint arXiv:2406.03295*, 2024.
- [41] Richard A Norte, Joao P Moura, and Simon Gröblacher. Mechanical resonators for quantum optomechanics experiments at room temperature. *Physical review letters*, 116(14):147202, 2016.
- [42] Christoph Reinhardt, Tina Müller, Alexandre Bourassa, and Jack C Sankey. Ultralow-noise sin trampoline resonators for sensing and optomechanics. *Physical Review X*, 6(2):021001, 2016.
- [43] WJ Venstra, HJR Westra, K Babaei Gavan, and HSJ Van Der Zant. Magnetomotive drive and detection of clamped-clamped mechanical resonators in water. *Applied Physics Letters*, 95(26), 2009.
- [44] Miao-Hsuan Chien, Johannes Steurer, Pedram Sadeghi, Nicolas Cazier, and Silvan Schmid. Nanoelectromechanical position-sensitive detector with picometer resolution. *ACS photonics*, 7(8):2197–2203, 2020.
- [45] Monica La Mura, Patrizia Lamberti, Vincenzo Tucci, Justinas Jorudas, Maria Cojocari, Georgy Fedorov, and Polina Kuzhir. Exploring the Impact of Absorber Material on the Performance of a Terahertz Microbolometer by Finite Element Analysis. In *2023 IEEE Nanotechnology Materials and Devices Conference (NMDC)*, pages 520–524, October 2023.
- [46] Mahsa Haddadi. M, Bamadev Das, Jeeyoon Jeong, Sunghwan Kim, and Dai-Sik Kim. Near-maximum microwave absorption in a thin metal film at the pseudo-free-standing limit. *Scientific Reports*, 12(1):18386, 2022.
- [47] Tommi Kaplas and Polina Kuzhir. Ultra-Thin Pyrocarbon Films as a Versatile Coating Material. *Nanoscale Res Lett*, 12(1):121, February 2017.
- [48] Tommi Kaplas and Yuri P. Svirko. Direct deposition of semitransparent conducting pyrolytic carbon films. *JNP*, 6(1):061703, October 2012.
- [49] Justinas Jorudas, Hamza Rehman, Maria Cojocari, Daniil Pashnev, Andrzej Urbanowicz, Irmantas Kašalynas, Benedetta Bertoni, Leonardo Vicarelli, Alessandro Pitanti, Sergei Malykhin, Yuri Svirko, Polina Kuzhir, and Georgy Fedorov. Ultra-broadband absorbance of nanometer-thin pyrolyzed-carbon film on silicon nitride membrane. *Nanotechnology*, 35(30):305705, May 2024.
- [50] David B Leeson. A simple model of feedback oscillator noise spectrum. *Proceedings of the IEEE*, 54(2):329–330, 1966.
- [51] Mark A Ordal, LL Long, Robert John Bell, SE Bell, RR Bell, Ralph William Alexander, and CA Ward. Optical properties of the metals al, co, cu, au, fe, pb, ni, pd, pt, ag, ti, and w in the infrared and far infrared. *Applied optics*, 22(7):1099–1119, 1983.
- [52] AG Golenkov and FF Sizov. Performance limits of terahertz zero biased rectifying detectors for direct detection. *Semiconductor physics quantum electronics & optoelectronics*, 2016.
- [53] Qinxi Qiu, Wanli Ma, Jingbo Li, Lin Jiang, Wangchen Mao, Xuehui Lu, Nianguan Yao, Yi Shi, and Zhiming Huang. High sensitivity of room-temperature terahertz photodetector based on silicon. *Science*, 25(10), 2022.
- [54] HW Hou, Z Liu, JH Teng, T Palacios, and SJ Chua. High temperature terahertz detectors realized by a gan high electron mobility transistor. *Scientific reports*, 7(1):46664, 2017.
- [55] Haowen Hou, Zhihong Liu, Jinghua Teng, Tomás Palacios, and Soo-Jin Chua. A sub-terahertz broadband detector based on a GaN high-electron-mobility transistor with nanoantennas. *Appl. Phys. Express*, 10(1):014101, November 2016.
- [56] Y. Kurita, G. Ducournau, D. Coquillat, A. Satou, K. Kobayashi, S. Boubanga Tombet, Y. M. Meziani, V. V. Popov, W. Knap, T. Suemitsu, and T. Otsuji. Ultrahigh sensitive sub-terahertz detection by InP-based asymmetric dual-grating-gate high-electron-mobility transistors and their broadband characteristics. *Applied Physics Letters*, 104(25):251114, June 2014.
- [57] K. Batrakov, P. Kuzhir, S. Maksimenko, A. Padubskaya, S. Voronovich, T. Kaplas, and Yu. Svirko. Enhanced microwave shielding effectiveness of ultrathin pyrolytic carbon films. *Applied Physics Letters*, 103(7):073117, August 2013.